The Effects of Orography on Midlatitude Northern Hemisphere Dry Climates

A. J. BROCCOLI AND S. MANABE

Geophysical Fluid Dynamics Laboratory/NOAA, Princeton University, Princeton, New Jersey

(Manuscript received 18 July 1991, in final form 13 February 1992)

ABSTRACT

The role of mountains in maintaining extensive midlatitude arid regions in the Northern Hemisphere was investigated using simulations from the GFDL Global Climate Model with and without orography. In the integration with mountains, dry climates were simulated over central Asia and the interior of North America, in good agreement with the observed climate. In contrast, moist climates were simulated in the same regions in the integration without mountains. During all seasons but summer, large amplitude stationary waves occur in response to the Tibetan Plateau and Rocky Mountains. The midlatitude dry regions are located upstream of the troughs of these waves, where general subsidence and relatively infrequent storm development occur and precipitation is thus inhibited. In summer, this mechanism contributes to the dryness of interior North America as a stationary wave trough remains east of the Rockies, but is not effective in Eurasia due to seasonal changes in the atmospheric circulation. The dryness of interior Eurasia in summer results, in part, from the south Asian monsoon circulation induced by the Tibetan Plateau. Its rising branch is centered above the southeastern Tibetan Plateau, and its salient features are a cyclonic flow at low levels (the "south Asian low") and an anticyclonic flow in the upper troposphere. This circulation is associated with a northward displacement of the storm track and a flow of relatively dry, subsiding air across much of central Asia. In addition, land surface–atmosphere feedback contributes to the dryness of all midlatitude dry regions. Although the effect of this feedback is small in winter, it is responsible for more than half of the reduction in summer precipitation. Orography also substantially reduces the moisture transport across the continental interiors. The results from this experiment suggest that midlatitude dryness is largely due to the existence of orography. This is an alternative to the traditional explanation that distance from oceanic moisture sources, accentuated locally by the presence of mountain barriers upwind, is the major cause of midlatitude dry regions. Paleoclimatic evidence of less aridity during the late Tertiary, before substantial uplift of the Rocky Mountains and Tibetan Plateau is believed to have occurred, supports this possibility.

1. Introduction

Our understanding of the mechanisms that control the global distribution of arid climates is incomplete. Widespread subtropical dry regions exist in northern Africa, the Middle East, Pakistan and northwestern India, the southwestern United States and Mexico, coastal Peru and Chile, southern Africa, and Australia. All of these regions lie in belts between 15° and 35° on either side of the equator, and are located beneath the subsiding branch of the Hadley circulation. But other sizeable dry regions exist across the interior of Asia from Turkestan east to the Gobi Desert, and in the western interior of North America from the Great Basin to the prairies of Canada and the Great Plains. These dry regions are not as readily explained by a simple schematic model of the global circulation, since they are located beneath the traveling disturbances of the Northern Hemisphere midlatitude westerlies.

A traditional explanation of midlatitude aridity is that the interiors of large continents are dry because of their distance from oceanic moisture sources, with the dryness accentuated in some locations by the presence of mountain barriers upwind (e.g., Haurwitz and Austin 1944; Crutchfield 1974; Trewartha and Horn 1980). If this explanation were sufficient, then midlatitude aridity (although perhaps less intense) would be expected even in the absence of orography. Atmospheric general circulation models (GCMs) provide a method of testing this hypothesis. A number of studies have been performed in which GCMs have been used to simulate the earth's climate with and without mountains (e.g., Mintz 1965; Kasahara and Washington 1971; Kasahara et al. 1973; Manabe and Terpstra 1974; Hahn and Manabe 1975; Lau 1986; Tokioka and Noda 1986; Kutzbach et al. 1989).

Some of the information resulting from these and other studies hints at the possibility that midlatitude aridity may be related to the presence of orography. Manabe and Terpstra (1974) briefly discussed the differences in the precipitation distribution based on simulations of the January climate with and without mountains. They found a zonal belt of moderate pre-

Corresponding author address: A. J. Broccoli, Geophysical Fluid Dynamics Laboratory, NOAA, Princeton University, Princeton, NJ 08542.

cipitation stretching across the midlatitudes of the Northern Hemisphere in the case without mountains and interruptions in this zonal belt over the interiors of Eurasia and North America in their experiment with mountains. Hahn and Manabe (1975) explored the role of mountains in the south Asian summer monsoon circulation. By comparing simulations with and without orography, they found that the south Asian monsoon circulation was greatly altered in their experiment without mountains and that the presence of the Tibetan Plateau was required for the northward expansion of the monsoon over India. Subsequently, using a model with orography and incorporating seasonal variation, Manabe and Holloway (1975) compared the simulated and observed distributions of global climate and found that their model simulated the midlatitude dryness of the Eurasian interior. They suggested that the Tibetan Plateau plays a major role in maintaining this dryness based on the results of the winter simulations of Manabe and Terpstra (1974) and the summer simulations of Hahn and Manabe (1975).

More recent work has suggested that changes in climate during the past 30–40 million years may be associated with large-scale uplift of the Tibetan Plateau and the western United States (Ruddiman and Kutzbach 1989). As part of this work, the National Center for Atmospheric Research Community Climate Model (NCAR CCM) has been used to run climate model experiments with and without mountains (Kutzbach et al. 1989). Perpetual January and July integrations were run in order to study changes in climate in both the summer and winter seasons. Substantial similarity exists between their January results and those of Manabe and Terpstra (1974), as well as between the response of the model to changes in orography and climatic changes in the geological record (Ruddiman and Kutzbach 1989).

With this evidence in place to suggest a connection between orography and the distribution of Northern Hemisphere midlatitude arid climates, an experiment was designed to investigate this possible connection and to explore the mechanisms that may be involved. While previous studies have examined the effects of orography from a variety of perspectives, this study will examine specifically the ability of the model to simulate midlatitude arid climates and the mechanisms, both atmospheric and hydrologic, by which those climates are maintained. This requires integrations that explicitly incorporate the annual cycle and include a land-surface model with interactive hydrology, conditions that were not met in previous studies. Early results from this work were presented by Manabe and Broccoli (1990). Further elaboration of their results is found in the sections that follow and includes an analysis of the mechanisms maintaining midlatitude aridity in summer and the effects of soil moisture feedback, topics that were discussed only briefly in that paper.

A detailed description of the model used and the experimental design is contained in sections 2 and 3. Section 4 examines the changes in the distribution and morphology of dry climates in response to changes in orography, while section 5 examines changes in large-scale circulation. The role of soil moisture feedback is explored in section 6, and the paleoclimatic implications of the current results are discussed in section 7. Concluding remarks are contained in section 8. The Appendix describes a parameterization of orographic gravity wave drag used in this experiment and its consequences for climate simulation.

2. Model description

A version of the climate model of the Geophysical Fluid Dynamics Laboratory (GFDL) similar to that of Manabe and Hahn (1981) was used in this study and consists of two basic units: 1) a general circulation model of the atmosphere, and 2) a heat and water balance model over the continents. The oceanic component of the climate system was not modeled explicitly; instead, the geographical distribution of sea surface temperature and sea ice was prescribed, varying seasonally, in a manner consistent with observations.

The atmospheric model employs the semispectral method in which the horizontal distributions of the primary variables are represented by spherical harmonics. The present model retains 30 zonal waves, adopting the so-called rhomboidal truncation. The spacing of the corresponding transform grid is 2.25° latitude by 3.75° longitude. Normalized pressure is used as the model's vertical coordinate, with nine unevenly spaced levels used for finite differencing. The dynamical component of this model was developed by Gordon and Stern (1982) and is very similar to that developed by Bourke (1974).

Solar radiation at the top of the atmosphere is prescribed, varying seasonally but not diurnally. Computation of the flux of solar radiation is performed using a method similar to that of Lacis and Hansen (1974), except that the bulk optical properties of various cloud types are specified. Terrestrial radiation is computed as described by Stone and Manabe (1968). For the computation of radiative transfer, clouds are prescribed, varying only with height and latitude. The mixing ratio of carbon dioxide is assumed constant everywhere, and that of ozone is specified as a function of height, latitude, and season.

Over the continents, surface temperatures are computed from a heat balance with the requirement that no heat is stored in the soil. Both snow cover and soil moisture are predicted. A change in snow depth is predicted as the net contribution from snowfall, sublimation, and snowmelt, with the latter two determined from the surface heat budget. Soil moisture is computed by the "bucket method." The soil is assumed to have a water-holding capacity of 15 cm. If the computed

soil moisture exceeds this amount, the excess is assumed to be runoff. Changes in soil moisture are computed from the rates of rainfall, evaporation, snowmelt, and runoff. Evaporation from the soil is determined as a function of soil moisture and the potential evaporation rate (i.e., the hypothetical evaporation rate from a completely wet soil). Further details of the hydrologic computations can be found in Manabe (1969).

An additional characteristic of the model is a parameterization of the drag that results from the breaking of orographically induced gravity waves. Parameterizations of this kind have been found to improve the performance of atmospheric GCMs for both weather forecasting and climate simulation (Palmer et al. 1986; McFarlane 1987). In the current experiments, gravity wave drag was used in all integrations where orography was present, and it substantially improves the simulation of midlatitude aridity. A description of this parameterization and a discussion of its impact on the simulation of climate are contained in the Appendix.

3. Experimental design

Three numerical integrations were run with the model as described in the previous section. In one of these integrations, realistic geography and topography were used, as depicted in Fig. 1. Since the geographical distribution of orography is represented by a limited number of spherical harmonics, it is very smooth. Despite this smoothness, most of the large-scale features of the global topography are represented, such as the Tibetan Plateau, the Rocky and Andes cordilleras, the East African highlands, and the Greenland and Antarctic ice sheets. This integration will subsequently be identified as the mountain (M) integration. The second integration used the same geographical distribution of land and sea as the M integration, but with flat continents. This integration will be identified as the no-mountain (NM) integration.

Comparing the results from these two integrations provides the response of the climate system (as represented by the model) to the presence of orography. A wide variety of interactions or feedbacks are included in the model, and thus, the response includes the effects of these interactions. A third integration, known as the fixed soil moisture (FSM) integration, was performed to evaluate one of these feedbacks—specifically, that between the land surface and the atmosphere. The FSM integration uses the same distribution of geography and topography as the M integration. Unlike the M integration, where it is predicted from a water balance, soil moisture at each grid point is prescribed, varying seasonally. The soil moisture values are based on the climatological values from the NM integration using the procedure employed by Delworth and Manabe (1989) in their prescribed soil moisture experiment.

All integrations were initiated from an isothermal, resting atmosphere and integrated until a quasi equilibrium was reached. Since sea surface temperature and sea ice were prescribed, only a relatively short spinup period was required. A period of three years subsequent to the achievement of quasi equilibrium was retained for analysis. Unless otherwise noted, the results presented herein utilize data from those three-year periods.

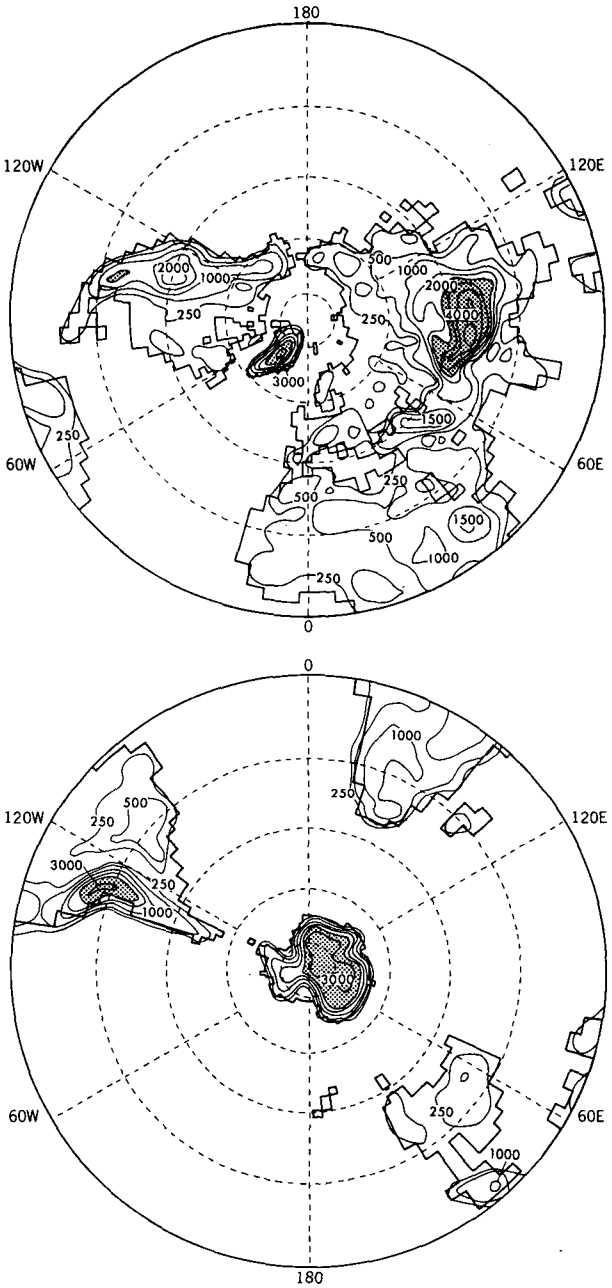

FIG. 1. Surface elevation (m) of topography used for the M integration. Top: Northern Hemisphere. Bottom: Southern Hemisphere. Stippled areas indicate elevations > 2000 m. Contours at 250, 500, 1000, 1500, 2000, 3000, 4000, and 5000 m. Due to spectral truncation, contours extend over oceans since model elevation is not constrained to be zero at ocean grid points.

By evaluating differences in climate between pairs of integrations, the total response of the climate system to orography can be examined as well as the contribution of soil moisture feedback to that response. A comparison between the M and NM integrations yields the total response of the climate system to orography, while a comparison between results from the FSM and NM integrations yields the response to orography without the feedback between the atmosphere and soil moisture. Accordingly, the difference between the M and FSM integrations represents the contribution of soil moisture feedback.

4. Distribution of dry climates

To provide an indication of the overall character of the climates simulated in the M and NM integrations, the output from these simulations was used to determine the Köppen climate classification at each grid point. In the Köppen system, monthly mean temperature and precipitation are used to classify climate in a manner designed to correspond to the prevailing natural vegetation. This commonly used climate classification scheme has previously been used to examine climates simulated by GCMs (Manabe and Holloway 1975; Guetter and Kutzbach 1990). A detailed description of the Köppen scheme can be found, for example, in Lamb (1972, pp. 509–514).

Köppen category B denotes desert and steppe climates, where precipitation is insufficient to meet the demands of forest vegetation at the prevailing temperatures. The spatial distributions of the B climates simulated by the M and NM integrations are depicted in Fig. 2, as is the observed distribution. In the NM integration, dry climates are confined to regions between 15° and 35° latitude in each hemisphere. These subtropical belts of aridity are nearly continuous, with only eastern China and the southeastern United States experiencing more moist climates. Midlatitude dryness is almost completely absent in the NM integration. This contrasts sharply with the results from the M integration in which the subtropical dry regions are not as extensive and substantial aridity occurs across the midlatitude interior of Eurasia and, to a lesser extent, North America. Comparison with the observed distribution of aridity indicates that the M integration is in good agreement over the midlatitude Northern Hemisphere, indicating that the model's simulation of temperature and precipitation in these regions is realistic.

Another measure of model aridity comes from the geographical distribution of annual mean soil moisture (Fig. 3). In the NM integration, little east–west variation of soil moisture occurs, although the east coasts of North America and Asia are somewhat wetter than the remainder of those continents. The pattern of soil moisture contours is largely zonal, with values in excess of 80% of saturation in northern regions of the continents and below 20% in the subtropics. This zonal symmetry is not so distinct in the M integration in which substantial east–west variation exists across both Eurasia and North America. While substantial regions of subtropical dryness are present, the zonality so evident in the NM integration is less dramatic. Of particular interest to this study are two midlatitude regions of soil dryness. One extends eastward from the Caspian Sea across central Asia into northwest China, while another lies just east of the Rocky Mountains in Canada and the northern United States.

The areas of low soil moisture correspond very well to the regions where Köppen's category B climates are simulated. This similarity occurs because both the soil moisture and the Köppen classification depend upon the relative magnitudes of the precipitation and potential evaporation. The Köppen scheme classifies arid and semiarid climates on the basis of an empirical relationship involving temperature and precipitation, using temperature as a surrogate indicator of the potential evaporation from the land surface. The B climates are those in which potential evaporation substantially exceeds precipitation. In the model, on an annual mean basis a balance must exist between the inflow to the soil moisture "bucket" (precipitation) and the outflow (evaporation and runoff). The evaporation E is related to the potential evaporation E_p by $E = \beta E_p$, where $\beta = \min(w/w_k, 1.0)$, with w the soil moisture and w_k an empirical value (chosen to be 11.75 cm, or 75% of field capacity) below which evaporation is limited by soil moisture. Thus, for $w < w_k$, the actual evaporation is smaller than the potential evaporation by a factor of w/w_k. Because annual mean precipitation and evaporation must balance (in regions of small runoff), this implies that potential evaporation exceeds precipitation wherever $w < w_k$. Thus, the regions that experience potential evaporation that greatly exceeds precipitation are those with low soil moisture.

The contrast between the largely zonal pattern of the NM integration and the more complex pattern of the M integration is present for annual mean precipitation (Fig. 4) as well as for soil moisture. Without orography, the smallest amounts occur over the Arctic Ocean and in two subtropical regions: southwestern North America and the adjacent Pacific, and northern Africa and the nearby Atlantic. Precipitation is relatively large in a band that circles the hemisphere between 45°N and 65°N and also at lower latitudes over the western North Atlantic and western North Pacific. In the M integration more east–west variability occurs at midlatitudes than in the NM integration, and precipitation is light over the continental interior regions where soil moisture is also low. In addition to the aforementioned regions of light precipitation over the Arctic Ocean and in the subtropics, annual precipitation rates of less than 1 mm d^{-1} extend across central Asia and in a band just east of the Rocky Mountains in North America. Comparison with the NM precip-

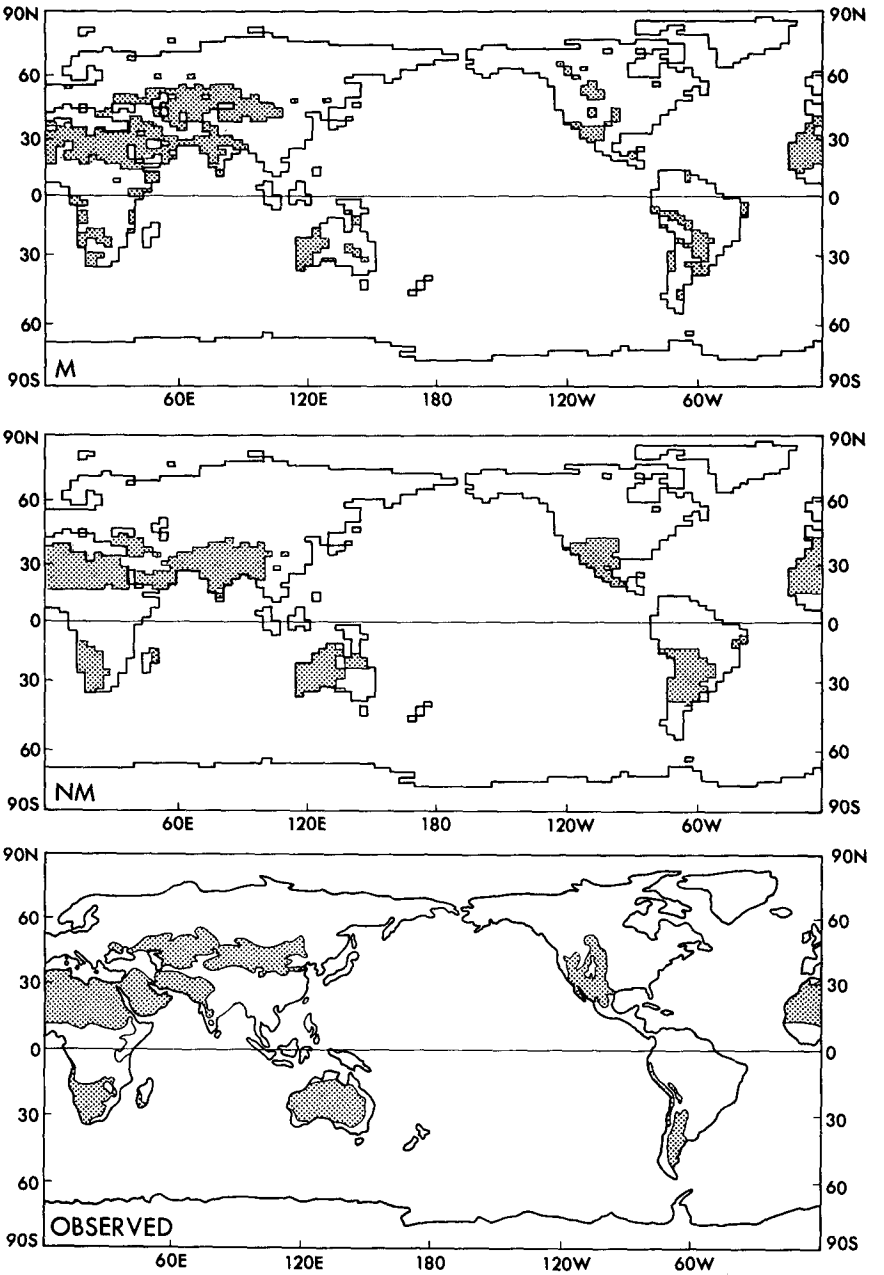

FIG. 2. Distribution of arid and semiarid climates according to the Köppen climate classification. Top: M integration. Center: NM integration. Bottom: observed (after Oliver 1973).

itation maps indicates large differences in annual precipitation across these areas.

To explore the seasonal variations of the difference in precipitation between the M and NM integrations, its annual march was computed for each of three regions: west-central Asia, east-central Asia, and the Canadian prairie (Fig. 5). The boundaries of these regions are depicted in Fig. 6. In all three areas precipitation in the M integration is substantially lower throughout the entire year than in the NM integration. The seasonal cycles of precipitation for the M integration are somewhat different in each region, with a late winter–early spring maximum in west-central Asia, a summer maximum in east-central Asia, and a spring maximum in the Canadian prairie. In the NM integration, the heaviest precipitation in all three regions occurs during the period March–June, with a secondary autumn maximum in west-central Asia and the Canadian prairie. While there is some disagreement between the annual march of precipitation from the M integration

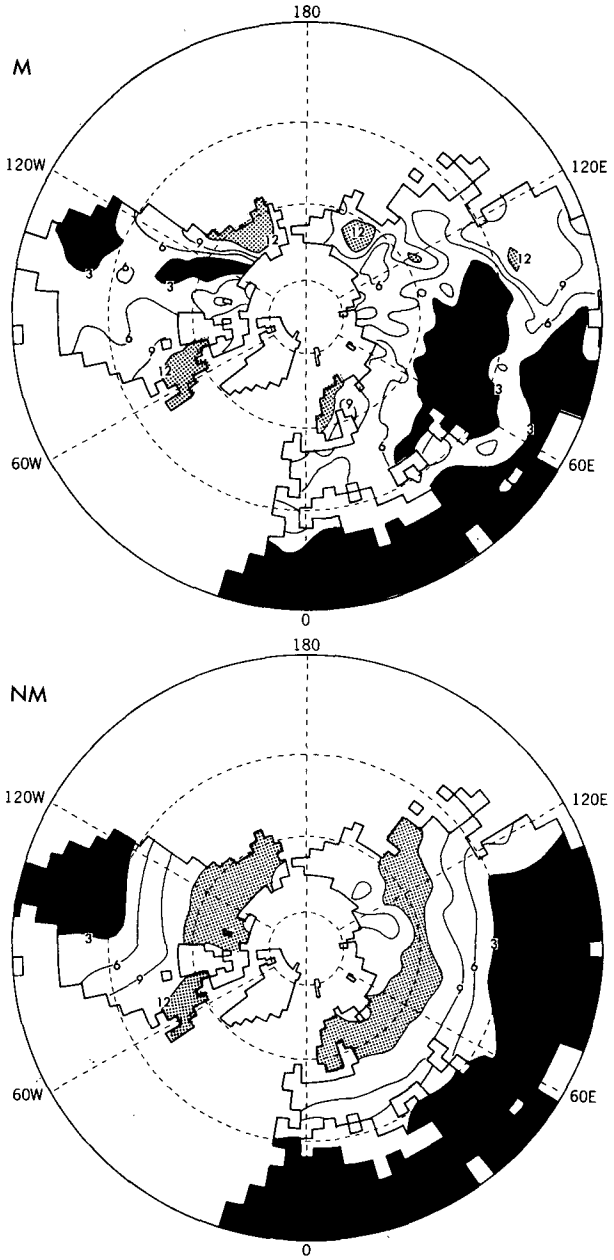

FIG. 3. Annual mean soil moisture (cm). Top: M integration. Bottom: NM integration. Stippling indicates soil moisture > 12 cm; solid black indicates soil moisture < 3 cm. The field capacity of soil moisture in both integrations is 15 cm everywhere. A 1-2-1 smoothing has been applied in both directions to reduce grid-scale variability.

and that observed (not shown) for west-central Asia and the Canadian prairie, these differences are typically smaller than the differences between the M and NM integrations.

5. Large-scale atmospheric circulation

The results of the previous section demonstrate a substantial decrease in precipitation over portions of the interiors of Eurasia and North America due to the presence of orography. What are the mountain-induced changes in circulation that produce this drying? A relatively simple and well-understood mechanism probably contributes to the dryness of the western interior of North America. As the prevailing lower-tropospheric westerlies encounter the Rocky Mountains, forced ascent with orographic precipitation occurs on the upwind side while subsidence occurs downwind. This so-

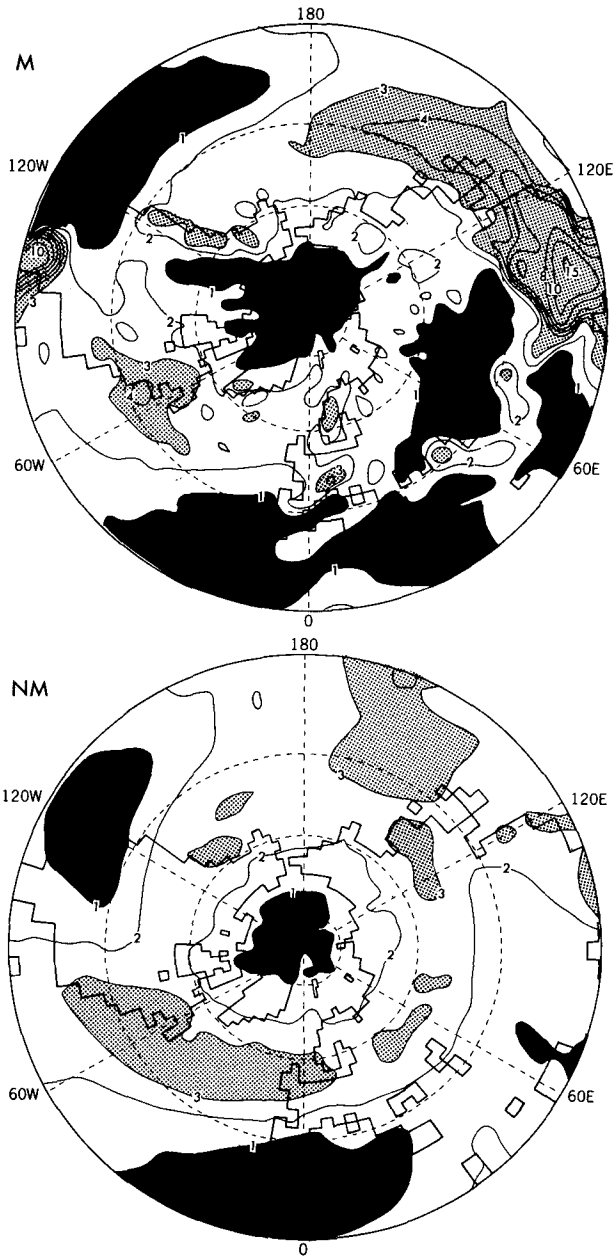

FIG. 4. Annual mean precipitation (mm d^{-1}). Top: M integration. Bottom: NM integration. Contours at 1, 2, 3, 4, 5, 6, 8, 10, 15, 20, and 30 mm d^{-1}. Stippling indicates precipitation > 3 mm d^{-1}; solid black indicates precipitation < 1 mm d^{-1}. Smoothing as in Fig. 3.

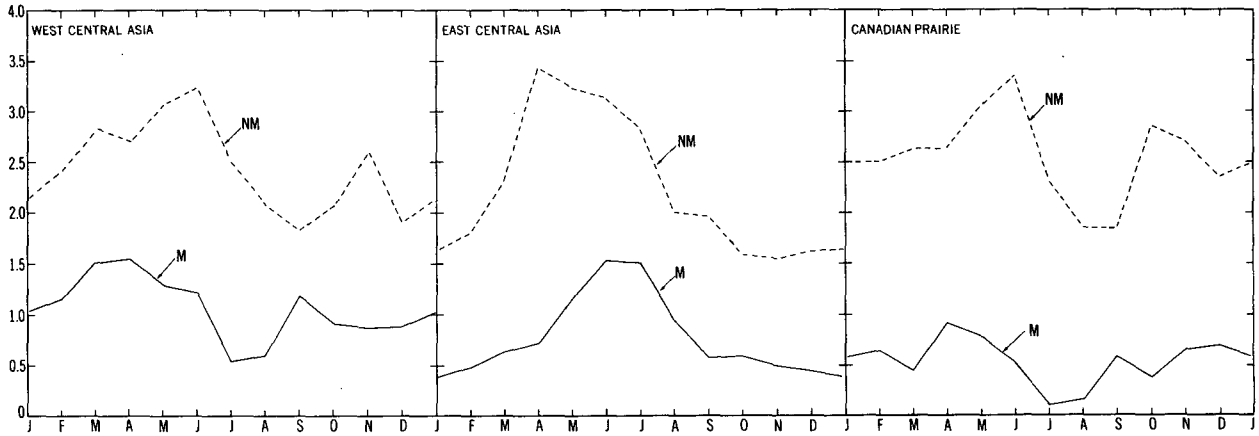

FIG. 5. Seasonal variation of monthly precipitation (mm d^{-1}) from the M and NM integrations for three regions. Left: west-central Asia. Center: east-central Asia. Right: Canadian prairie.

called "rain shadow" effect cannot satisfactorily explain the dryness of central Asia, since that continent lacks an extensive meridional barrier such as the Rocky Mountains. Other mechanisms must be involved in maintaining the arid climate of the Eurasian interior, and these mechanisms contribute to the dryness of western interior North America as well.

Atmospheric disturbances propagating along the polar front are responsible for much of the precipitation in middle latitudes, particularly during the cold season. The preferred locations for disturbance activity are related to stationary waves in the upper troposphere, as Blackmon et al. (1977) found in their analysis of the observed winter circulation in the Northern Hemisphere. Theoretical studies (e.g., Bolin 1950; Nigam et al. 1988) have indicated that stationary waves can result from orographic influences. Thus, it is possible that orographically induced stationary waves, by determining the regions of frequent (infrequent) passage of extratropical disturbances and ascent (subsidence), may influence the climatological distribution of precipitation strongly enough to explain the existence of midlatitude dry regions.

a. Spring

Because the continental precipitation belts in the NM integration are best defined in the spring season, the March–May circulation will be examined first to explore this hypothesis. A variety of diagnostics of the atmospheric circulation at the 500-mb level will be examined. They include the geopotential height (depicting the stationary waves), isotachs (for identification of jet streams), and the root-mean-square (rms) of the geopotential height bandpass filtered to retain fluctuations with time scales between 2.5 and 6 days (a measure of synoptic-scale disturbance activity). The 500-mb level is chosen since Blackmon et al. (1977) and Blackmon and Lau (1980) have found the rms of bandpass-filtered heights at that level to correspond well with synoptic disturbances. While higher tropospheric levels may be equally, or more, suitable for identifying the stationary wave pattern and jet-stream locations, comparison of upper-tropospheric maps with those from the 500-mb level suggests that the features are similar.

The geopotential heights and isotachs (Fig. 7, top) indicate that stationary waves have relatively small amplitudes in the NM integration and that a circumpolar jet axis circles the Northern Hemisphere at between 45° and 50°N. In contrast to this zonally sym-

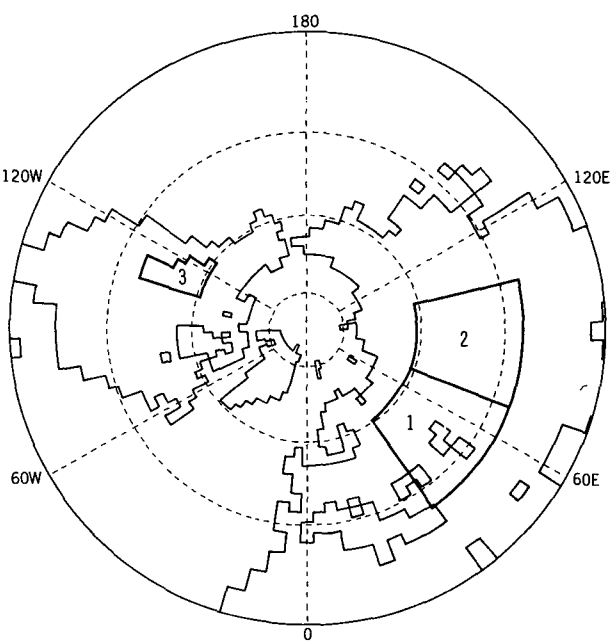

FIG. 6. Areas used in computation of regional precipitation: 1) west-central Asia; 2) east-central Asia; 3) Canadian prairie. Only land points within these regions were used in the computations.

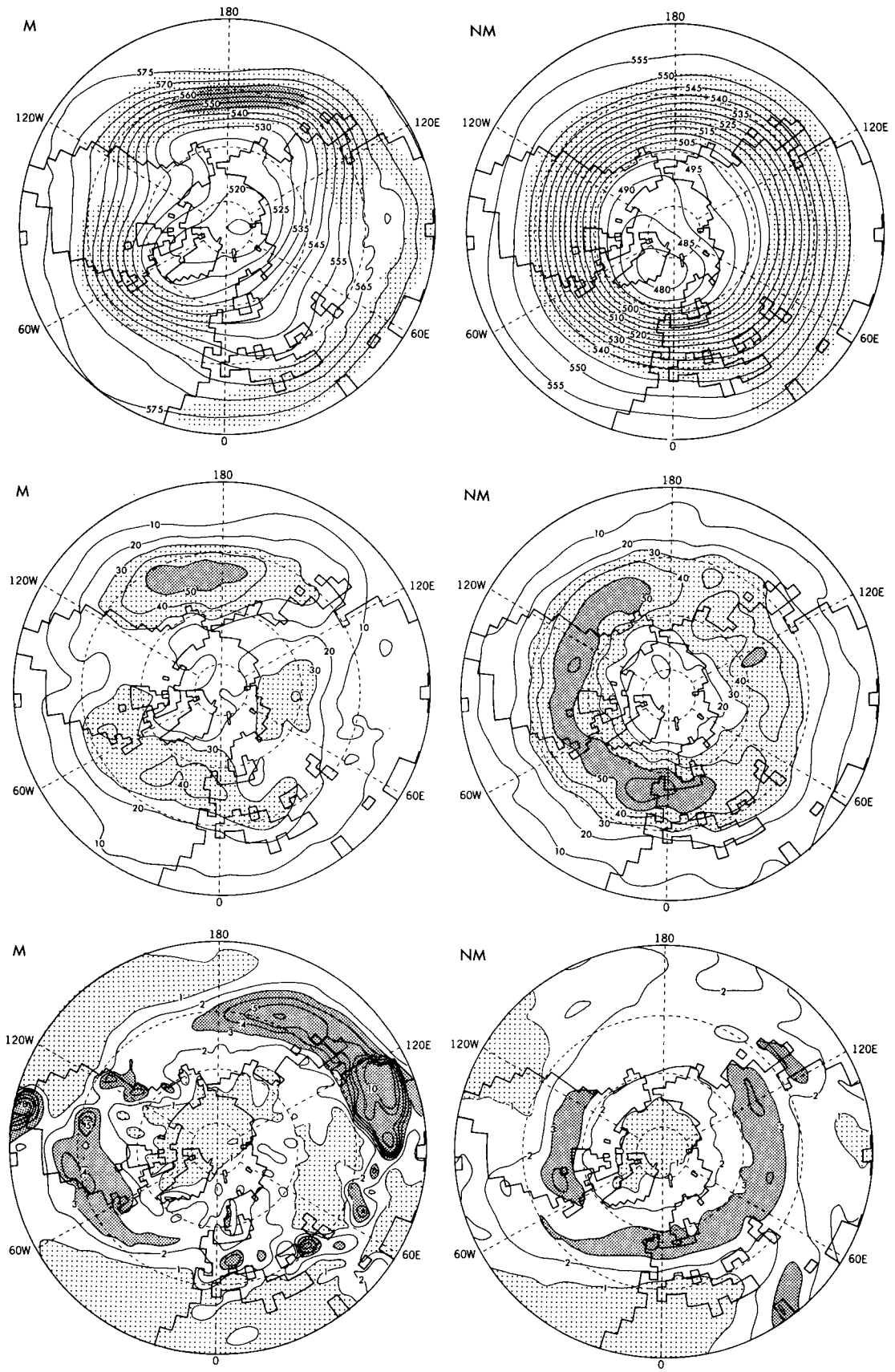
M
NM
180
120W
120E
60W
60E
0

metric picture, stationary waves in the M integration have rather large amplitudes, with troughs situated downstream of the Tibetan Plateau and Rocky Mountains. Each of these troughs is associated with a wind maximum located downstream. Manabe and Terpstra (1974) and Kutzbach et al. (1989) noted a similar increase in the amplitude of stationary waves in the presence of orography.

Contrasting patterns between the M and NM integrations are also noted in the rms of bandpass-filtered 500-mb heights (Fig. 7, center). In the NM integration, a circumpolar band of high synoptic disturbance activity lies between 50° and 55°N, or just poleward of the maximum 500-mb winds. In the M integration, the bands of high disturbance activity are more narrowly confined to the maxima stretching across the North Pacific and North Atlantic. These storm tracks also closely parallel the corresponding 500-mb wind maxima that occur downstream of the trough axes. Manabe and Terpstra (1974) also noted a close association between storm tracks and jet axes in their GCM simulation. Substantially lower rms values occur over the regions of midlatitude aridity in the M integration than in the same locations in the NM integration, indicating a reduction in synoptic disturbance activity.

The spring precipitation distributions (Fig. 7, bottom) from the M and NM integrations resemble the annual means (Fig. 4). In the NM integration, a band of moderate precipitation circles the hemisphere between 45° and 60°N, with the heaviest amounts over the continents exceeding 3 mm d^{-1}. This rain belt nearly coincides with the axis of maximum 500-mb winds and storminess. Elsewhere there are modest departures from zonal symmetry as discussed in regard to the annual mean precipitation maps. In the M integration, large departures from zonal symmetry occur in middle latitudes, with precipitation rates less than 1 mm d^{-1} across central Asia. Smaller areas with less than 1 mm d^{-1} are present east of the Canadian Rockies. Over these regions, precipitation in the M integration is as little as one-third of that in the NM integration.

A picture emerges in which a clear relationship between midlatitude precipitation and stationary waves is evident in the M integration. Precipitation tends to be heaviest in the areas downstream of the stationary wave troughs, such as from the east coast of North America east-northeastward across the North Atlantic and from China across Japan into the North Pacific. These regions of heavy precipitation are closely aligned with large synoptic disturbance activity and relatively strong midtropospheric winds. The time-averaged vertical pressure velocity pattern (Fig. 8), while rather noisy, is indicative of large-scale ascent in these regions. In areas upstream of the troughs, synoptic disturbance

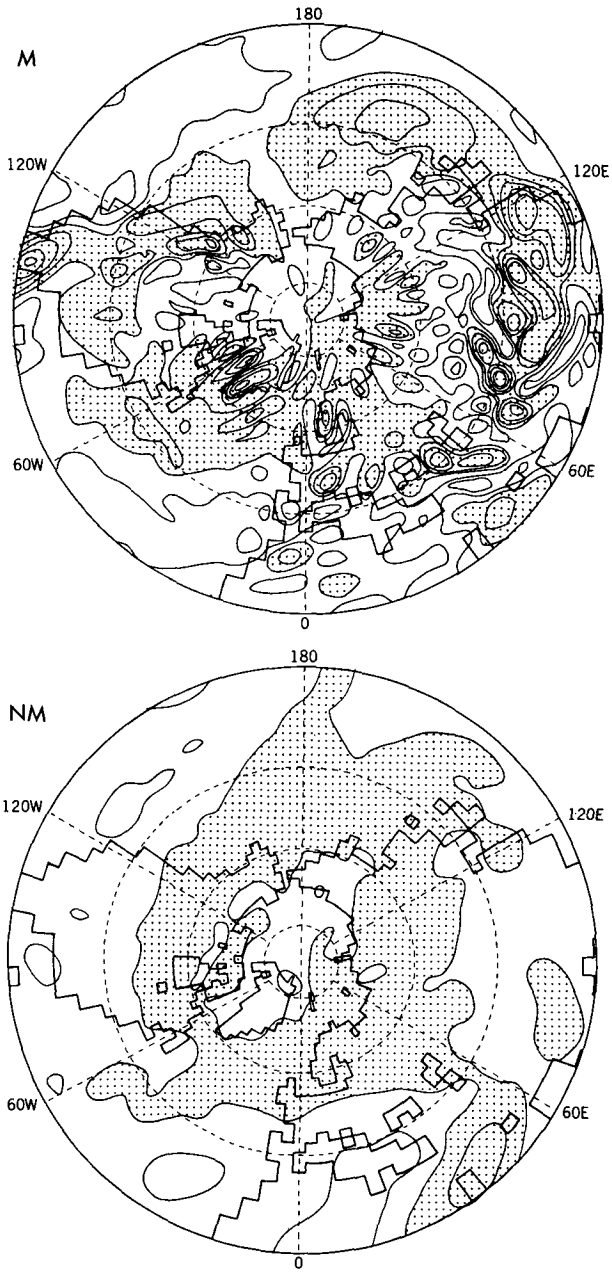

FIG. 8. March–April–May vertical pressure velocity (dyn cm^{-2} s^{-1}) at the 515-mb level. Contour interval 0.25 dyn cm^{-2} s^{-1}. Stippling indicates negative values (i.e., upward motion). Top: M integration. Bottom: NM integration. Smoothing as in Fig. 3.

FIG. 7. March–April–May circulation and precipitation from the (left) M integration and (right) NM integration. Top: 500-mb geopotential height (dm). Light stippling indicates 500-mb winds > 12 m s^{-1}; dense stippling > 24 m s^{-1}. Center: Root-mean-square (rms) of bandpass-filtered 500-mb geopotential height (m). The bandpass filter selects disturbances between 2.5 and 6 days. Light stippling indicates values > 30 m; dense stippling > 50 m. Bottom: Precipitation (mm d^{-1}). Light stippling indicates precipitation < 1 mm d^{-1}; dense stippling > 3 mm d^{-1}. Contour interval as in Fig. 4, and smoothing as in Fig. 3.

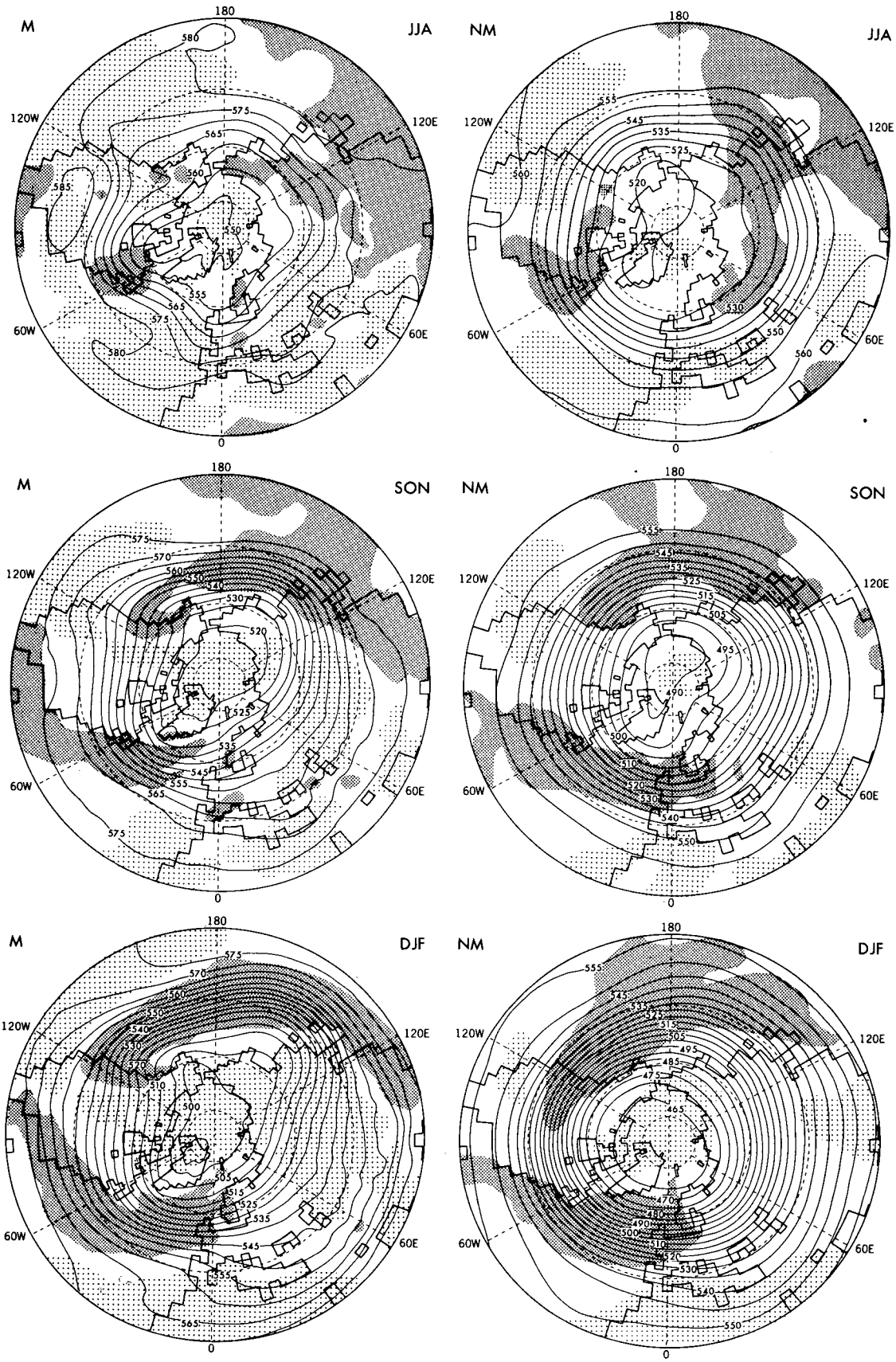
M
JJA
NM
JJA
M
SON
NM
SON
M
DJF
NM
DJF
180
120W
120E
60W
60E
0

activity is relatively weak and precipitation is light, with general subsidence prevailing. In the more zonally symmetric NM integration, stationary wave amplitudes are small, so that precipitation and disturbance activity is associated with a circumpolar jet axis that is continuous around the hemisphere. Time-averaged vertical velocities are much weaker than in the M integration.

b. Autumn and winter

Composite maps of 500-mb height and precipitation for autumn and winter from the NM integration (Fig. 9, right) reveal relatively low amplitude departures from zonal symmetry. As in spring, the maximum precipitation in middle latitudes occurs beneath the strongest westerlies. The largest precipitation rates in this belt occur primarily over the oceans, with modest penetration into western North America and Europe. In the M integration, the 500-mb circulation (Fig. 9, left) during autumn and winter is qualitatively similar to that of spring. Large amplitude stationary waves occupy similar positions, although their amplitudes vary with season, as does the intensity of the zonal circulation. The belts of heavy precipitation extending from the east coasts of Asia and North America east-northeastward are present in these seasons as well as spring, and extensive areas of low precipitation (less than 1 mm d^{-1}) are present in the continental interiors. Thus, the overall relationship between midlatitude precipitation and stationary waves can be generalized to include autumn and winter as well.

c. Summer

In summer, the 500-mb circulation in the NM integration (Fig. 9, top right) maintains its generally zonal character. The midlatitude rain belt associated with this westerly flow is quite prominent over the continents. Summer also brings relatively heavy rainfall at lower latitudes over the east coasts of North America and Asia. These are regions that lie under southerly flow on the west side of the oceanic anticyclones, which reach their northernmost latitudes in summer. During summer, the stationary wave pattern in the M integration (Fig. 9, top left) is quite different from other seasons in both the wave amplitudes and positions. While a trough remains over eastern North America, the east Asian trough is not present. This is reasonable, since the westerlies have retreated far enough north that they no longer encounter the Tibetan Plateau. Despite this change, extensive dryness still prevails over central Asia, particularly west of 100°E, where the axis of a weak trough is located. Since this trough is absent in the NM experiment, it must be the result of orographic forcing, either direct or indirect. The summer precipitation difference between the M and NM integrations in this region is substantial, with drier conditions prevailing in the M experiment.

Previous work points to another kind of orographically induced circulation change as a possible source of the reduction in summer precipitation. In their GCM simulations with and without orography, Hahn and Manabe (1975) found that mountains played a large role in the south Asian monsoon circulation. They found that a center of rising motion was present above the Tibetan Plateau and its southern slope in the integration with mountains but was absent from the same location in the integration without mountains. Since the south Asian monsoon is the dominant circulation in the region, it is reasonable to expect that some of the differences in central Asian summer precipitation between the NM and M integrations could be due to the changes in this circulation.

The velocity potential at the 205-mb level for northern summer provides a large-scale indication of these changes in the current experiment. Bearing in mind that the divergent component of the flow is along the gradient of velocity potential, a minimum (maximum) in this quantity is associated with large-scale divergence (convergence) at that level. In the NM integration (Fig. 10, center) a dipole pattern is evident, with an elongated minimum over the western tropical Pacific and Southeast Asia and a maximum over the tropical Atlantic. The heavy precipitation falling from Southeast Asia eastward along the equatorial region suggests the importance of latent heating in maintaining this circulation. A similar dipole pattern is also present in the M integration (Fig. 10, top), but the primary center of the elongated minimum is shifted west-northwestward to Southeast Asia, where precipitation is very heavy. In the difference map (Fig. 10, bottom) a strong minimum is located above the southeast portion of the Tibetan Plateau, indicative of increased upper divergence at that location. An area of enhanced precipitation coincides with this center, consistent with the orographically induced enhancement of the south Asian monsoon first noted by Hahn and Manabe (1975).

The intense latent heating above the southeast portion of the Tibetan Plateau produces a distinctive warm core structure, with a low-level cyclonic circulation (the "monsoon low" or "south Asian low") beneath an anticyclonic circulation in the upper troposphere. The divergence associated with the upper-tropospheric anticyclone can be inferred from the velocity potential map. While proximity to the elevated surface produces some irregularities in the flow, the lower-tropospheric

FIG. 9. 500-mb geopotential height (dm) from the (left) M integration and (right) NM integration. Light stippling indicates precipitation < 1 mm d^{-1}; dense stippling precipitation > 3 mm d^{-1}. Top: June–July–August. Center: September–October–November. Bottom: December–January–February.

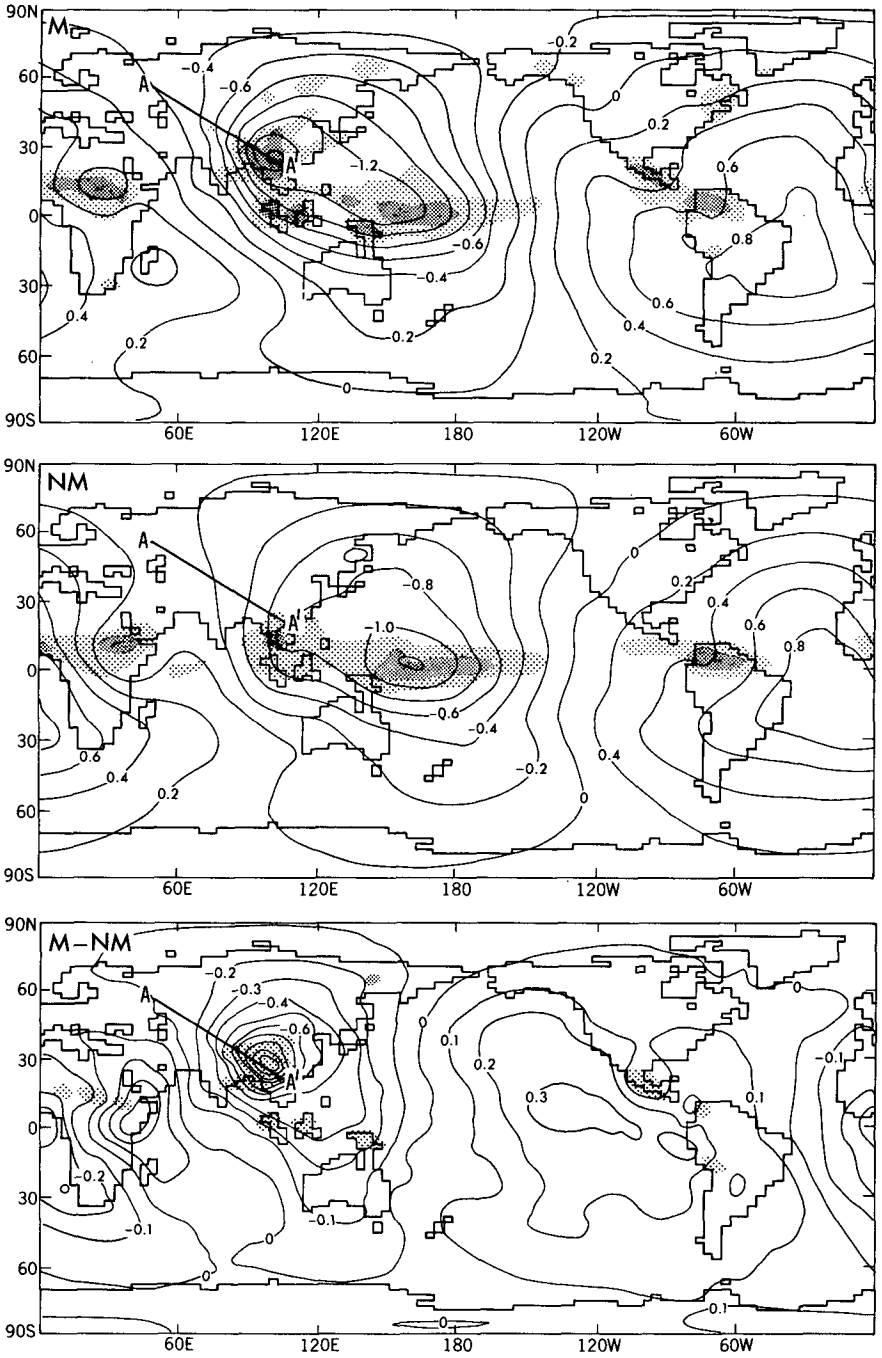

FIG. 10. June–July–August 205-mb velocity potential (10^7 m^2 s^{-1}). Top: M integration. Center: NM integration. Bottom: M minus NM. Light stippling indicates precipitation between 5–10 mm d^{-1}; dense stippling precipitation > 10 mm d^{-1}. In bottom panel, stippling indicates precipitation increase > 4 mm d^{-1}. The lines AA′ in the top and center panels depict the orientation of the cross section shown in Fig. 12.

cyclonic circulation is evident in a map of wind vectors at the 830-mb level and height contours at the 850-mb level from the M integration (Fig. 11, top). The circulation associated with this center of upper divergence and low-level convergence is evident in a cross section of vertical pressure velocity (Fig. 12, top) extending from northwest to southeast across the Tibetan Plateau along the line indicated on Fig. 10. Intense upward motion occurs above the southeast portion of the plateau and its vicinity as southwesterly winds in the lower

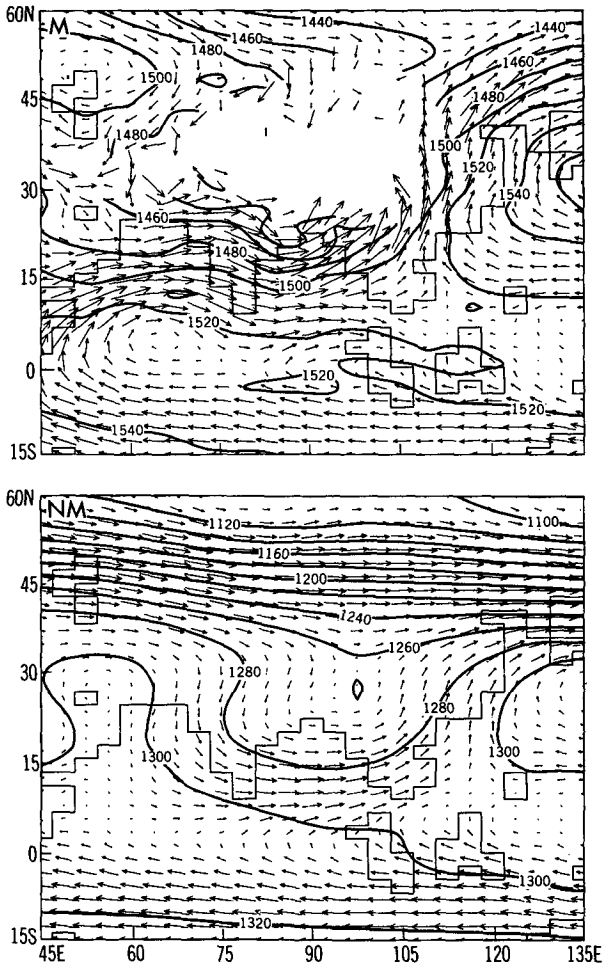

FIG. 11. Wind vectors at 830-mb level with contours of geopotential height (m) at 850 mb superimposed. No vectors or contours are plotted if the appropriate level is below the surface. Top: M integration. Bottom: NM integration.

troposphere (Fig. 11, top) encounter its southern slope. To the northwest of the Tibetan Plateau strong subsidence occurs. A similar vertical velocity pattern was identified by He et al. (1987) in their analysis of FGGE data for an 80-day period surrounding the onset of the 1979 summer monsoon. They attributed the ascent over the Tibetan Plateau and descent over nearby areas to its west and north to the vertical circulation induced by the plateau.

In association with the low-level cyclonic circulation, the meridional component of the lower-tropospheric flow is equatorward in the area north of the Tibetan Plateau, so that relatively dry air that subsides northwest of the Tibetan Plateau is carried across those portions of central Asia north and west of the plateau. To the south, the northward flow of air from the Indian Ocean and subcontinent does not penetrate beyond the Tibetan Plateau. This contrasts with the NM integration, where strong lower-tropospheric westerlies occur over middle latitudes, extending equatorward to the latitude of the Tibetan Plateau (Fig. 11, bottom). The south Asian low is largely absent, with only a weak trough over Southeast Asia in its place. In addition, strong centers of vertical velocity are absent from south Asia (Fig. 12, bottom).

An active storm track, indicated by the rms of band-pass-filtered 500-mb height (Fig. 13, bottom), is associated with the midlatitude westerlies of the NM integration, which extend upward throughout the entire depth of the troposphere. The disturbances propagating along this track bring substantial precipitation to central Asia. By contrast, the low-level cyclonic circulation surrounding the Tibetan Plateau in the M integration weakens the westerlies in the region north of the plateau, so that the strongest winds in the lower troposphere are weaker and shifted poleward. A corresponding change in the storm track occurs, with the band of maximum synoptic disturbance activity weakened and shifted northward (Fig. 13, top). The combination of subsidence, the low-level flow of dry air, and this reduction of storminess is unfavorable for precipitation over central Asia.

d. Water vapor transport

The impact of orography on midlatitude aridity can be viewed from another perspective by examining the

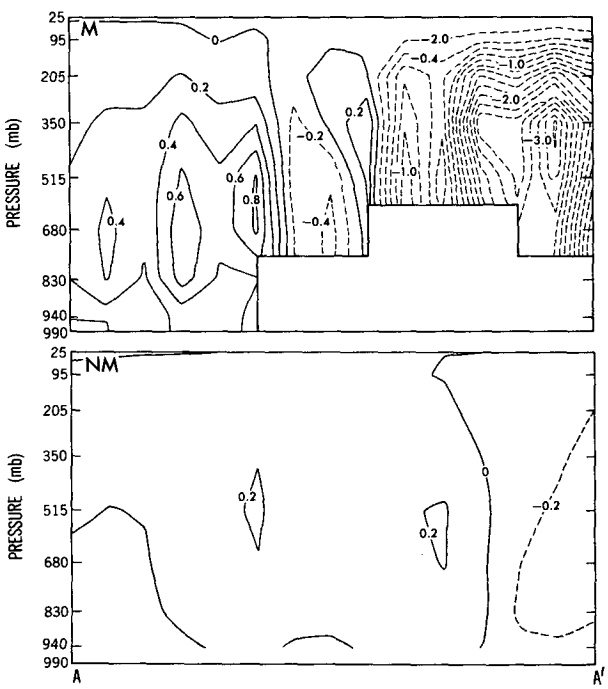

FIG. 12. Cross section of vertical pressure velocity (dyn cm^{-2} s^{-1}) along the line depicted in Fig. 10. A 1–2–1 smoothing has been applied to the geographical distribution of vertical pressure velocity at each level before forming the cross section. Dashed contours indicate negative values (i.e., upward motion). Top: M integration. Bottom: NM integration.

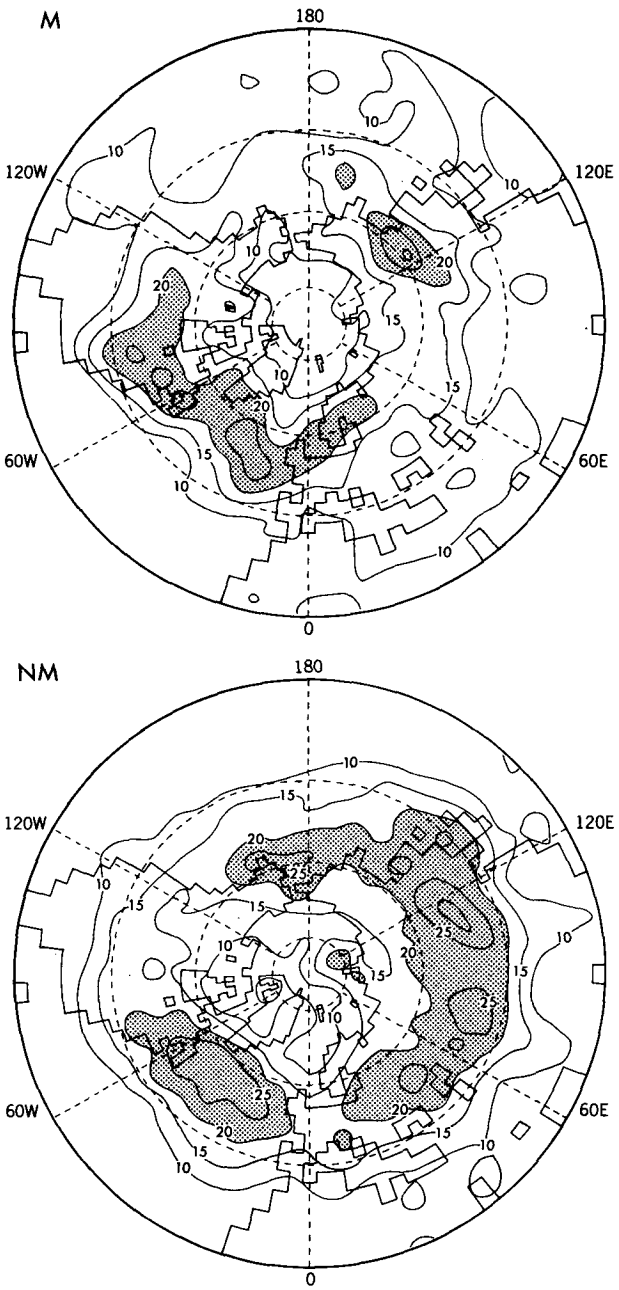

FIG. 13. Root-mean-square of bandpass-filtered 500-mb geopotential height (m) for the June–July–August season. Values greater than 20 m are stippled. Top: M integration. Bottom: NM integration.

annual mean vertically integrated water vapor transport from the model integrations. Assuming that no net change in moisture storage in the atmosphere or soil occurs, a condition generally met when averaging over an annual cycle, the divergence of this transport is equal to the difference between evaporation and precipitation. Due to data processing limitations, the moisture transport was computed using only one year of data from each experiment, but given the large changes in boundary conditions and of the model's response to those changes, it is likely that the differences are representative of what would have been obtained from a longer sample.

In the NM integration (Fig. 14, bottom), a strong flow of moisture prevails throughout the belt from 40° through 60°N, carrying an ample supply of moisture from oceanic sources to the continents. Anticyclonic circulations centered over the eastern North Pacific, central North Atlantic, and northern Arabian Sea carry

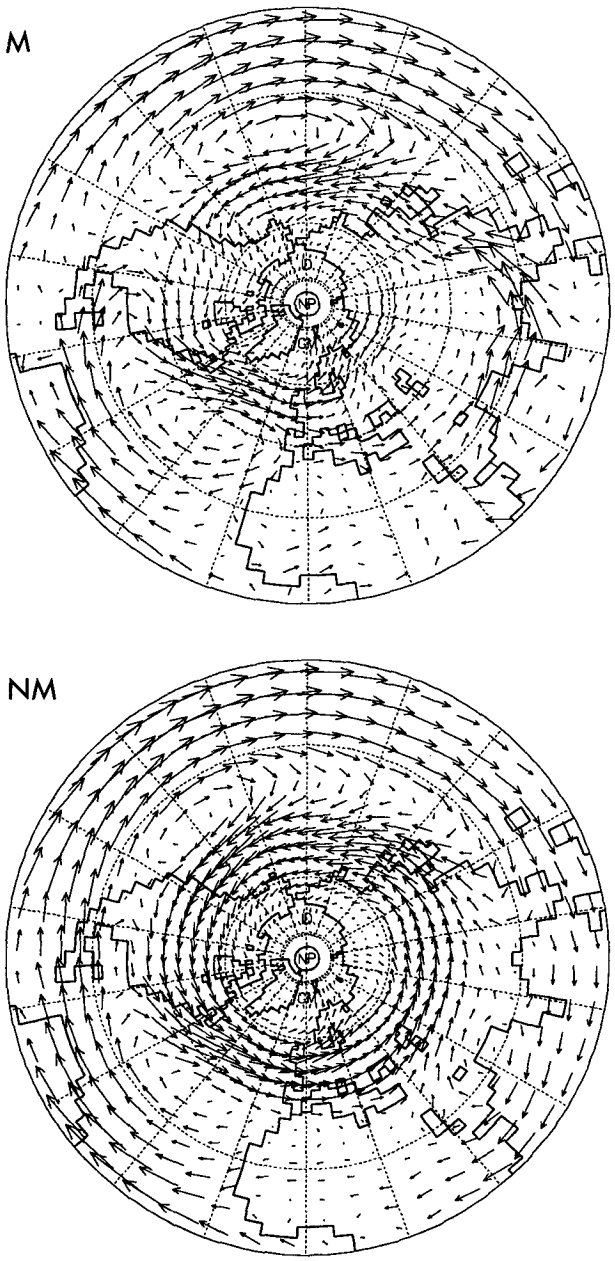

FIG. 14. Annual average vertically integrated water vapor transport vectors. Top: M integration. Bottom: NM integration.

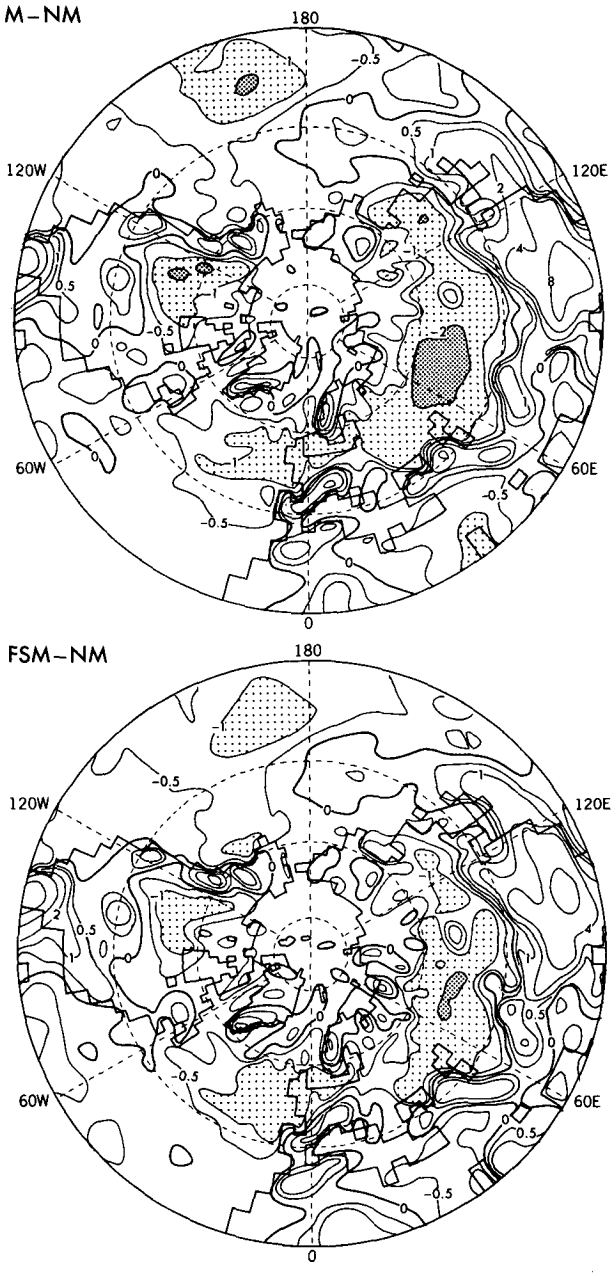

FIG. 15. Annual mean precipitation difference (mm d^{-1}). Top: M minus NM. Bottom: FSM minus NM. Contours at −2, −1, −0.5, 0, 0.5, 1, 2, 4, and 8 mm d^{-1}. Light stippling indicates precipitation difference between −1 and −2 mm d^{-1}; dense stippling < −2 mm d^{-1}. Smoothing as in Fig. 3.

moisture from the tropics into this westerly transport stream. In addition, moisture penetrates deep into the interiors of North America and Eurasia. The high soil moisture values of the NM integration may promote this penetration by allowing moisture to be recycled through the land surface, since evaporation from the relatively wet soil takes place at a substantial fraction of the potential rate.

Strong westerly transport also occurs across the North Atlantic and North Pacific in the M integration (Fig. 14, top) in a manner similar to the NM integration, but this flow weakens as it enters North America and Europe. Over the Eurasian continent, a bifurcation of the moisture flow is evident, with westerly transport over the extreme north and across the Middle East, India, and Southeast Asia, bypassing the continental interior. Thus, the effect of orography is to substantially reduce the water vapor transport into the interior regions of both North America and Eurasia.

6. Role of soil moisture feedback

In the results presented thus far, the response of the model to orography has included the effect of soil moisture–atmosphere interaction. A number of climate model studies (e.g., Rind 1982; Yeh et al. 1983; Delworth and Manabe 1989) have demonstrated that this interaction can be quite important. In the context of the present experiment, soil moisture feedback would operate in the following manner. The presence of orography can induce, for example, a decrease in precipitation. Through the alteration of the water budget, this reduction in precipitation results in a decrease in soil moisture. If there is sufficient radiative energy available at the surface, the reduction in soil moisture can lead to a decrease in evaporation from the surface. This lowers the atmospheric humidity, leading to an additional decrease in precipitation. (As described in this hypothetical example, the feedback would be positive.)

To explore the role of soil moisture feedback in the response of the present model to orography, the FSM integration was included in this study. As described in section 3, this integration used the topography of the M integration but had soil moisture prescribed based on the NM integration. Differences between the FSM and NM integrations represent the effects of orography without soil moisture feedback, while differences between the M and NM integrations include soil moisture feedback.

The difference in annual mean precipitation between the M and NM integrations (Fig. 15, top) illustrates the large reduction of precipitation over the midlatitude continental interiors in a belt approximately between 40° and 60°N. A vast area experiences a decrease in precipitation rate larger than 1 mm d^{-1}, with decreases of more than 2 mm d^{-1} in central Asia and in small areas of western Canada. This pattern is largely reproduced in the annual mean precipitation differences between the FSM and NM integrations (Fig. 15, bottom), although the magnitudes of the precipitation reduction are somewhat smaller. This indicates that, for the annual mean response, the effect of soil moisture feedback is modest compared to that associated with the alteration of the atmospheric circulation.

This is confirmed by computing differences in annual precipitation for each of the three regions defined

an annual basis, soil moisture feedback is responsible for between one-fourth and one-third of the reduction in precipitation due to orography over the midlatitude arid regions. The contribution of this feedback undergoes a large seasonal variation, ranging from nearly zero in winter to more than half of the total response in summer, in accord with the changes in radiative energy available at the surface. The land surface acts as an agent that allows the decrease in cold season precipitation due to orographic stationary wave forcing to contribute to a reduction in precipitation during subsequent months. In addition to the positive feedback involving soil moisture and precipitation during summer itself, this is likely to be an important factor.

The results from these integrations suggest an alternative to the traditional explanation that distance from oceanic moisture sources, combined with local effects from the presence of mountain barriers upwind, are the major causes of midlatitude dry climates. While "rain shadow" effects undoubtedly contribute to the dryness of western interior North America and, perhaps to a lesser extent, the Gobi Desert, no sizeable mountain barriers lie upstream of the vast area of dryness east of the Caspian Sea. Thus, it seems reasonable to argue that mountains are responsible for the existence of these dry regions, acting through large-scale effects on the atmospheric circulation. The relative wetness of the continents in the experiment without orography suggests that large continents alone may not ensure the existence of midlatitude arid regions in their interiors.

Paleoclimatic evidence (i.e., vegetation changes, windborne dust) of less aridity in the northern Great Plains and central Asia during the late Tertiary may support this possibility. Ruddiman et al. (1989) hypothesize that many of the large-scale changes in land surface elevation in the western United States and the Tibetan Plateau region are geologically recent and could have substantial climatic effects as suggested by experiments with the NCAR CCM (Ruddiman and Kutzbach 1989; Kutzbach et al. 1989). If we accept the evidence for geologically recent uplift, the consistency of our results with the paleoclimatic data lends credence to our hypothesis for the maintenance of midlatitude aridity.

Some caution, however, is advised. Explanations other than recent uplift have been offered for this geological evidence (Molnar and England 1990). If that is the case, the paleoclimatic evidence of drying of the midlatitude interiors during the late Tertiary may not be as relevant to our results. In addition, we have found that an adequate simulation of midlatitude aridity depends on the details of the model used, so that a discernibly poorer simulation occurs with lower horizontal resolution or without the parameterization of gravity wave drag.

Despite these caveats our results seem to be relatively robust. While these climate model integrations used prescribed cloudiness, a comparison of the M integration with a corresponding integration with predicted cloudiness indicates that cloud feedback has little effect on the simulation of midlatitude dry regions. In addition, our results are consistent with those from other studies of orographic effects using different GCMs and simple linear models. This gives us some confidence that the mechanisms we have identified may largely account for midlatitude aridity.

Acknowledgments. We are especially grateful to Y. Hayashi for developing the orographic gravity wave drag parameterization used in this study and his assistance in preparing the Appendix. We also thank K. Cook, I. Held, N.-C. Lau, J. Mahlman, and the anonymous reviewers for their careful reviews of earlier drafts of this paper. I. Held deserves particular thanks for the insights provided to us during many discussions during the course of this work. The illustrations were prepared by P. Tunison and the Scientific Illustration Group at GFDL.

APPENDIX

The Orographic Gravity Wave Drag Parameterization And Its Effects On Climate

The parameterization of orographic gravity wave drag used in this experiment was developed by Y. Hayashi (private communication) based on linear theory.

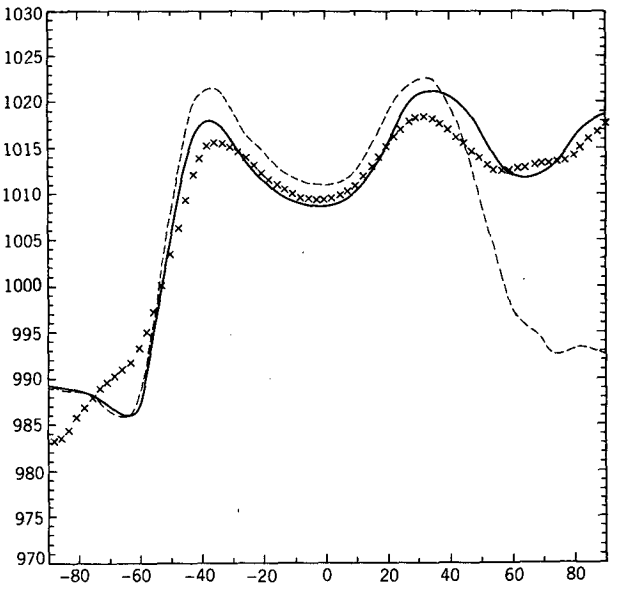

FIG. A1. Latitudinal distribution of December–January–February zonal average sea level pressure (mb) from the M integration (solid line) and the NG integration (dashed line). The observed data of Oort (1983) are shown for comparison (crosses).

The equations involved in the implementation of this parameterization follow. Only the equations for the zonal wind component (u) are listed; the equations for the meridional component (v) are of the same form.

The surface stress due to gravity wave drag $(\tau_0)_x$ is assumed to be

$$(\tau_0)_x = -N_{\text{low}}\rho_{\text{low}}k_0\overline{(h')^2}u_{\text{low}}, \quad (1)$$

where N_{low} is the Brunt–Väissälä frequency, ρ_{low} is the air density, k_0 is the representative mountain wavenumber (the representative mountain wavelength L_0 is $2\pi/k_0$), $\overline{(h')^2}$ is the subgrid-scale mountain height variance, and u_{low} the u-component wind. The model uses σ coordinates, where $\sigma = P/P_{\text{sfc}}$, P is the pressure, and P_{sfc} is the surface pressure. The subscript low indicates that the quantity is a mass-weighted average over the lowest three finite-difference levels ($\sigma = 0.83$, 0.94, and 0.99) of the model. The stress due to gravity wave drag at any level $\tau(\sigma)$ is calculated by simply assuming the following prescribed vertical distribution

$$\tau_x(\sigma) = \begin{cases} \dfrac{(\sigma - \sigma_c)}{(1 - \sigma_c)}(\tau_0)_x, & \sigma_c \leq \sigma \leq 1 \\ 0, & \sigma < \sigma_c \end{cases}, \quad (2)$$

where the critical level σ_c is defined as the lowest level at which $(uu_{\text{low}} + vv_{\text{low}}) \leq 0$. This means that the basic flow, assumed to be parallel to the surface flow, vanishes at this level. This scheme for vertically distributing the stress differs from those used by Palmer et al. (1986) and McFarlane (1987) and has been chosen for its simplicity. A similar scheme was employed by Laursen and Eliasen (1989), and has also been used in an operational model at the United Kingdom Meteorological Office (Palmer et al. 1986).

The effect of gravity wave drag enters as a term on the right-hand side of the tendency equation for u

$$\frac{\partial u}{\partial t} = \cdots + \frac{g}{P_{\text{sfc}}}\frac{\partial \tau(\sigma)}{\partial \sigma}. \quad (3)$$

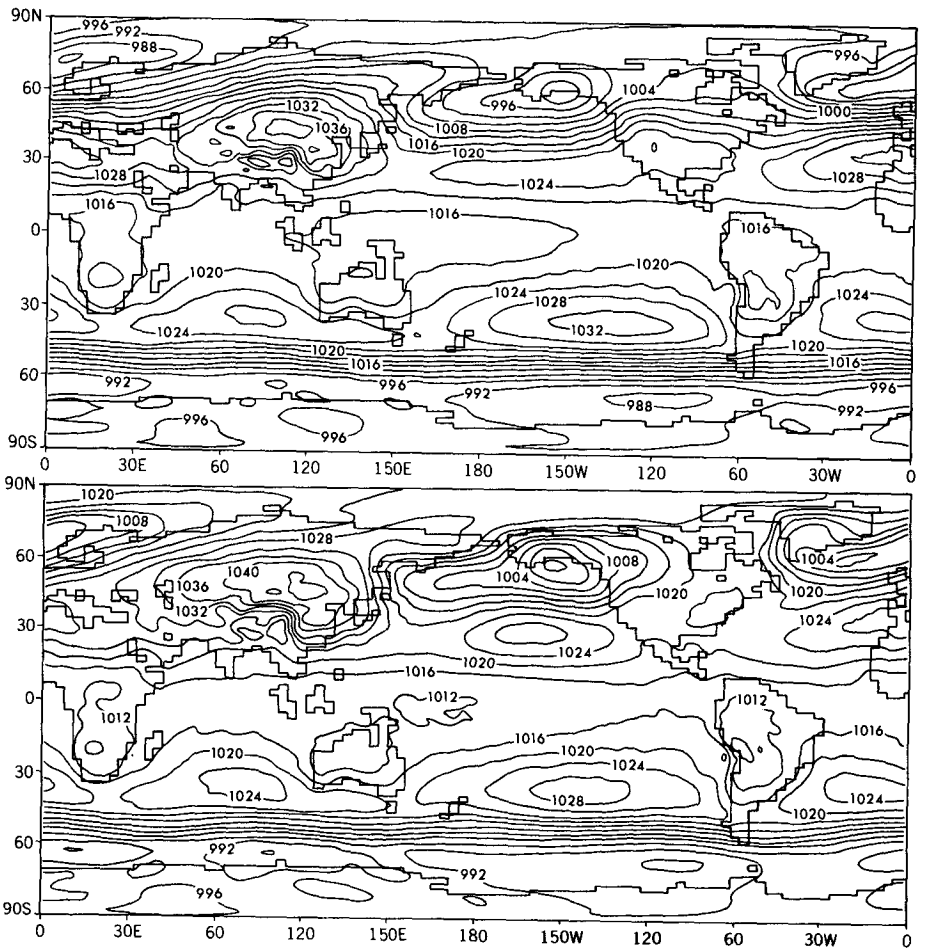

FIG. A2. December–January–February sea level pressure (mb).
Top: NG integration. Bottom: M integration.

For levels at or below the critical level, the tendency due to gravity wave drag can be computed by substituting (1) into (2) and differentiating, yielding

$$\frac{g}{P_{\text{sfc}}}\frac{\partial \tau_x(\sigma)}{\partial \sigma} = -\frac{g\rho_{\text{low}}N_{\text{low}}k_0\overline{(h')^2}u_{\text{low}}}{P_{\text{sfc}}(1-\sigma_c)}. \quad (4)$$

In the development of this parameterization, k_0 was estimated as 2.8×10^{-5} m^{-1} based on a high-resolution topographic dataset. When tested with this value of k_0, the gravity wave drag parameterization was found to excessively weaken the Northern Hemisphere winter midlatitude surface westerlies, as estimated from the meridional gradient of the zonal-mean sea level pressure. The value of k_0 was reduced to 2.2×10^{-5} m^{-1}, which yielded a more realistic latitudinal profile of sea level pressure. This value, which corresponds to a representative mountain wavelength of approximately 285 km, was used in all subsequent experiments using this parameterization.

To examine the impact of the orographic gravity wave drag parameterization on the simulation of climate, results from two integrations were compared: the M integration (as described in the main text), and a second integration identical except for the absence of gravity wave drag (the NG integration). The latitudinal distribution of the zonally averaged sea level pressure (SLP) for boreal winter (Fig. A1) illustrates the problem that the addition of gravity wave drag was designed to remedy. There is excellent agreement between the NG integration and the observed SLP (Oort 1983) in all of the Southern Hemisphere and in the low latitudes of the Northern Hemisphere. Poleward of 30°N, the latitude of the zonal mean subtropical ridge, the NG integration has an unrealistically large meridional gradient of SLP. This "westerly bias" was identified by Manabe et al. (1979) in early tests of the sensitivity of the GFDL GCM to horizontal resolution and is also evident in the geographical distribution of SLP (Fig. A2, top).

With gravity wave drag, a more realistic distribution of SLP is simulated in the M integration. The Aleutian low, Siberian high, and Icelandic low (the main "centers of action" of the winter circulation) are more clearly separated from each other. Substantial areas of meridional flow are present between these pressure systems. Absent is the very pronounced belt of strong westerlies that extends across the Northern Hemisphere continents in the NG integration. The excellent agreement between the simulated and observed SLP gradient in the Northern Hemisphere is not fortuitous, since the gravity wave drag formulation was tuned to reproduce the pressure gradient in these latitudes. Little change in the SLP pattern occurs in the Southern Hemisphere, in part due to the less extensive sources of orographically induced gravity waves in that hemisphere. This is desirable, since the Southern Hemisphere SLP simulation was realistic without gravity wave drag. Gravity wave drag also has little effect in summer in both hemispheres due to the smaller values for N_{low} and u_{low} during that season.

A comparison of the annual mean precipitation from the NG integration (Fig. A3, top) with that from the M integration (Fig. 4, top) indicates sizeable differences (Fig. A3, bottom). Substantial decreases in precipita-

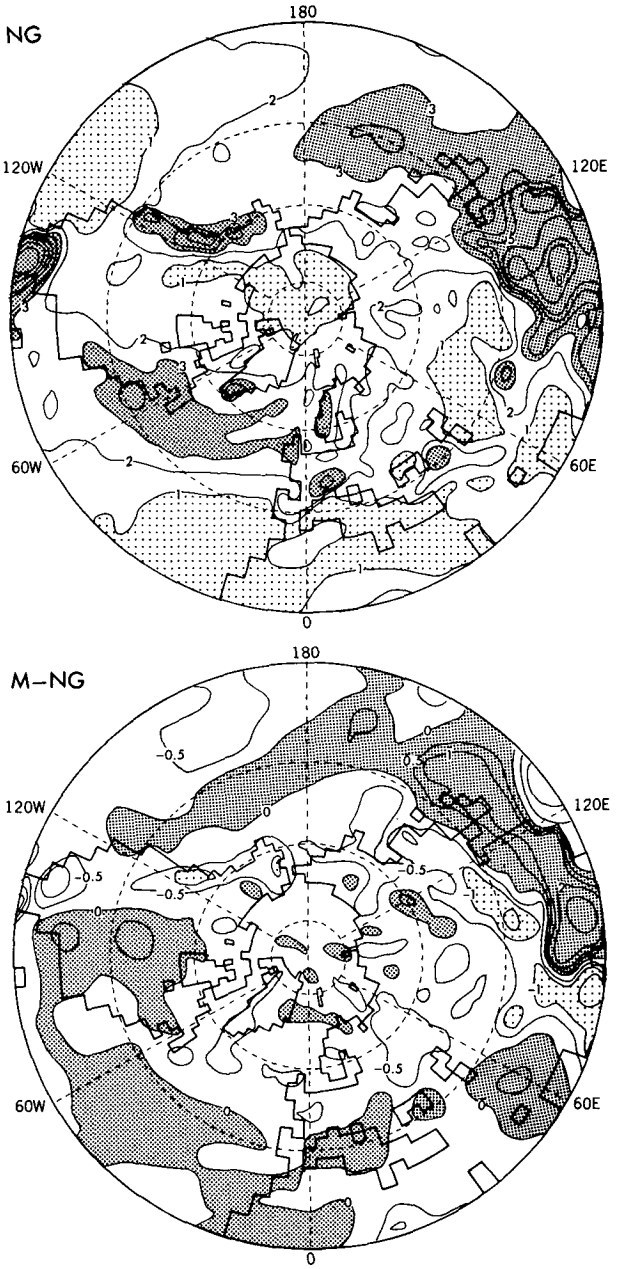

FIG. A3. Annual mean precipitation (mm d^{-1}). Top: NG integration; contours as in Fig. 4. Light stippling indicates precipitation < 1 mm d^{-1}; dense stippling > 3 mm d^{-1}. Bottom: M minus NG. Contours as in Fig. 13. Dense stippling indicates precipitation difference > 0; light stippling < −1 mm d^{-1}. Smoothing in both panels as in Fig. 3.

tion occur over many continental areas, particularly in Eurasia, in response to the inclusion of gravity wave drag. The midlatitude dry regions increase in area, as evident from the expansion of the area with precipitation rates less than 1 mm d^{-1}. A decrease in precipitation is also noted over the mountains of western Canada, where the westerly flow impinging on the Rocky Mountains decreases in intensity in the M integration with an attendant decrease in upslope precipitation. Although these changes in precipitation are instrumental in enabling a more realistic simulation of the midlatitude dry climates of the Northern Hemisphere, they account for only about one-fourth of the total precipitation change in these regions between the M and NM integrations.

REFERENCES

Blackmon, M. L., and N. -C. Lau, 1980: Regional characteristics of the Northern Hemisphere wintertime circulation: A comparison of the simulation of a GFDL general circulation model with observations. *J. Atmos. Sci.*, **37**, 497–514.

——, J. M. Wallace, N. -C. Lau, and S. L. Mullen, 1977: An observational study of the Northern Hemisphere wintertime circulation. *J. Atmos. Sci.*, **34**, 1040–1053.

Bolin, B., 1950: On the influence of the earth's orography on the general character of the westerlies. *Tellus*, **2**, 184–195.

Bourke, W., 1974: A multi-level model: 1. Formulation and hemispheric integrations. *Mon. Wea. Rev.*, **102**, 687–701.

Crutchfield, H. J., 1974: *General Climatology.* Prentice-Hall, 446 pp.

Delworth, T. L., and S. Manabe, 1989: The influence of soil wetness on near-surface atmospheric variability. *J. Climate*, **2**, 1447–1462.

Gordon, C. T., and W. F. Stern, 1982: A description of the GFDL global spectral model. *Mon. Wea. Rev.*, **110**, 625–644.

Guetter, P. J., and J. E. Kutzbach, 1990: A modified Koppen classification applied to model simulations of glacial and interglacial climates. *Clim. Change*, **16**, 193–215.

Hahn, D. G., and S. Manabe, 1975: The role of mountains in the south Asian monsoon circulation. *J. Atmos. Sci.*, **32**, 1515–1541.

Haurwitz, B., and J. M. Austin, 1944: *Climatology.* McGraw-Hill, 410 pp.

He, H., J. W. McGinnis, Z. Song, and M. Yanai, 1987: Onset of the summer monsoon in 1979 and the effect of the Tibetan Plateau. *Mon. Wea. Rev.*, **115**, 1966–1995.

Kasahara, A., and W. M. Washington, 1971: General circulation experiments with a six-layer NCAR model, including orography, cloudiness and surface temperature calculations. *J. Atmos. Sci.*, **28**, 657–701.

——, T. Sasamori, and W. M. Washington, 1973: Simulation experiments with a 12-layer stratospheric global circulation model: I. Dynamical effect of the earth's orography and thermal influence of continentality. *J. Atmos. Sci.*, **30**, 1229–1251.

Kutzbach, J. E., P. J. Guetter, W. F. Ruddiman, and W. L. Prell, 1989: Sensitivity of climate to late Cenozoic uplift in southern Asia and the American west: Numerical experiments. *J. Geophys. Res.*, **94**, 18 393–18 407.

Lacis, A. A., and J. E. Hansen, 1974: A parameterization for the absorption of solar radiation in the earth's atmosphere. *J. Atmos. Sci.*, **31**, 118–133.

Lamb, H. H., 1972: *Climate: Present, Past and Future. Vol. 1.* Methuen, 613 pp.

Lau, N. -C., 1986: The influences of orography on large-scale atmospheric flow simulated by a general circulation model. *Proc. of Int. Symp. on the Qinghai-Xizang Plateau and Mountain Meteorology,* Amer. Meteor. Soc., 241–269.

Laursen, L., and E. Eliasen, 1989: On the effects of the damping mechanisms in an atmospheric general circulation model. *Tellus*, **41A**, 385–400.

Manabe, S., 1969: Climate and the ocean circulation: I. The atmospheric circulation and the hydrology of the earth's surface. *Mon. Wea. Rev.*, **97**, 739–774.

——, and T. B. Terpstra, 1974: The effects of mountains on the general circulation of the atmosphere as identified by numerical experiments. *J. Atmos. Sci.*, **31**, 3–42.

——, and J. L. Holloway, Jr., 1975: The seasonal variation of the hydrologic cycle as simulated by a global model of the atmosphere. *J. Geophys. Res.*, **80**, 1617–1649.

——, and D. G. Hahn, 1981: Simulation of atmospheric variability. *Mon. Wea. Rev.*, **109**, 2260–2286.

——, and A. J. Broccoli, 1990: Mountains and arid climates of middle latitudes. *Science*, **247**, 192–195.

——, D. G. Hahn, and J. L. Holloway, Jr., 1979: Climate simulations with GFDL spectral models of the atmosphere: Effect of spectral truncation. *GARP Publ. Ser.*, No. 22, 41–94.

McFarlane, N. A., 1987: The effect of orographically excited gravity wave drag on the general circulation of the lower stratosphere and troposphere. *J. Atmos. Sci.*, **44**, 1775–1800.

Mintz, Y., 1965: Very long-term global integration of the primitive equations of atmospheric motion. WMO Tech. Note No. 66, 141–167.

Molnar, P., and P. England, 1990: Late Cenozoic uplift of mountain ranges and global climate change: Chicken or egg? *Nature*, **346**, 29–34.

Nigam, S., I. M. Held, and S. W. Lyons, 1988: Linear simulation of the stationary eddies in a GCM. Part II: The "mountain" model. *J. Atmos. Sci.*, **45**, 1433–1452.

Oliver, J. E., 1973: *Climate and Man's Environment.* Wiley and Sons, 517 pp.

Oort, A. H., 1983: Global atmospheric circulation statistics. NOAA Prof. Paper 14, U.S. Dept. of Commerce, NOAA, 180 pp.

Palmer, T. N., G. J. Shutts, and R. Swinbank, 1986: Alleviation of a westerly bias in general circulation and numerical weather prediction models through an orographic gravity wave drag parameterization. *Quart. J. Roy. Meteor. Soc.*, **112**, 1001–1039.

Rind, D., 1982: The influence of ground moisture conditions in North America on summer climate as modeled in the GISS GCM. *Mon. Wea. Rev.*, **110**, 1487–1494.

Ruddiman, W. F., and J. E. Kutzbach, 1989: Forcing of late Cenozoic Northern Hemisphere climate by plateau uplift in southern Asia and the American west. *J. Geophys. Res.*, **94**, 18 409–18 427.

——, W. L. Prell, and M. E. Raymo, 1989: Late Cenozoic uplift in southern Asia and the American west: Rationale for general circulation modeling experiments. *J. Geophys. Res.*, **94**, 18 379–18 391.

Stone, H. M., and S. Manabe, 1968: Comparison among various numerical models designed for computing infrared cooling. *Mon. Wea. Rev.*, **96**, 735–741.

Tokioka, T., and A. Noda, 1986: Effects of large-scale orography on January atmospheric circulation: A numerical experiment. *J. Meteor. Soc. Japan*, **64**, 819–839.

Trewartha, G. T., and L. H. Horn, 1980: *An Introduction To Climate.* McGraw-Hill, 416 pp.

Yeh, T. -C., R. T. Wetherald, and S. Manabe, 1983: A model study of the short-term climatic and hydrologic effects of sudden snowcover removal. *Mon. Wea. Rev.*, **111**, 1013–1024.